Signatures of large-scale cold fronts in the optically-selected merging cluster HSC J085024+001536

Keigo Tanaka,[1,*] **Ryuichi Fujimoto,**[2] **Nobuhiro Okabe** (ID) **,**[3,4,5]
Ikuyuki Mitsuishi,[6] **Hiroki Akamatsu,**[7] **Naomi Ota** (ID) **,**[8]
Masamune Oguri,[9,10,11] **and Atsushi J. Nishizawa**[12]

[1]Graduate School of Natural Science & Technology, Kanazawa University, Kakuma-machi, Kanazawa, Ishikawa 920-1192, Japan

[2]Faculty of Mathematics and Physics, Kanazawa University, Kakuma-machi, Kanazawa, Ishikawa 920-1192, Japan

[3]Physics Program, Graduate School of Advanced Science and Engineering, Hiroshima University, 1-3-1 Kagamiyama, Higashi-Hiroshima, Hiroshima 739-8526, Japan

[4]Hiroshima Astrophysical Science Center, Hiroshima University, 1-3-1 Kagamiyama, Higashi-Hiroshima, Hiroshima 739-8526, Japan

[5]Core Research for Energetic Universe, Hiroshima University, 1-3-1 Kagamiyama, Higashi-Hiroshima, Hiroshima 739-8526, Japan

[6]Graduate School of Science, Division of Particle and Astrophysical Science, Nagoya University, Furo-cho, Chikusa-ku, Nagoya, Aichi 464-8602, Japan

[7]SRON Netherlands Institute for Space Research, Sorbonnelaan 2, 3584 CA Utrecht, the Netherlands

[8]Department of Physics, Nara Women's University, Kitauoyanishi-machi, Nara, Nara 630-8506, Japan

[9]Department of Physics, The University of Tokyo, 7-3-1 Hongo, Bunkyo, Tokyo 113-0033, Japan

[10]Research Center for the Early Universe, The University of Tokyo, 7-3-1 Hongo, Bunkyo, Tokyo 113-0033, Japan

[11]Kavli Institute for the Physics and Mathematics of the Universe (Kavli IPMU, WPI), The University of Tokyo, 5-1-5 Kashiwanoha, Kashiwa, Chiba 277-8583, Japan

[12]Institute for Advanced Research, Nagoya University, Furocho, Chikusa-ku, Nagoya, Aichi 464-8602 Japan

*E-mail: tanaka@astro.s.kanazawa-u.ac.jp

Abstract

We represent a joint X-ray, weak-lensing, and optical analysis of the optically-selected merging cluster, HSC J085024+001536, from the Subaru HSC-SSP survey. Both the member galaxy density and the weak-lensing mass map show that the cluster is composed of south-east and north-west components. The two-dimensional weak-lensing analysis shows that the south-east component is the main cluster, and the sub-cluster and main cluster mass ratio is $0.32^{+0.75}_{-0.23}$. The north-west sub-cluster is offset by $\sim$700 kpc from the main cluster center, and their relative line-of-sight velocity is $\sim$1300 km s^{-1} from spectroscopic redshifts of member galaxies. The X-ray emission is concentrated around

the main cluster, while the gas mass fraction within a sphere of $1'$ radius of the sub-cluster is only $f_{\text{gas}} = 4.0^{+2.3}_{-3.3}\%$, indicating that the sub-cluster gas was stripped by ram pressure. An X-ray residual image shows three arc-like excess patterns, of which two are symmetrically located at $\sim$550 kpc from the X-ray morphological center, and the other is close to the X-ray core. The excess close to the sub-cluster has a cold-front feature where dense-cold gas and thin-hot gas contact. The two outer excesses are tangentially elongated about $\sim$450–650 kpc, suggesting that the cluster is merged with a non-zero impact parameter. Overall features revealed by the multi-wavelength datasets indicate that the cluster is at the second impact or later. Since the optically-defined merger catalog is unbiased for merger boost of the intracluster medium, X-ray follow-up observations will pave the way to understand merger physics at various phases.

1 Introduction

Cluster mergers are the most energetic phenomena in the Universe. Along with a large energy release, cluster mergers have a significant impact on both the thermal history and cluster evolution (e.g., Ricker & Sarazin 2001; ZuHone 2011) through shock waves induced by supersonic motions of sub-clusters. Subsonic motions trigger perturbations in the intracluster medium (ICM) distribution of main clusters and mix the two different ICMs of the main cluster and the sub-cluster (e.g., Ascasibar & Markevitch 2006; ZuHone et al. 2010). The feature of the mixing is sometimes observed as cold fronts (e.g., Markevitch & Vikhlinin 2007; Zuhone & Roediger 2016). The merging process can be broadly divided into three phases of pre-merger, on-going, and post-merger by a sound-crossing time scale. The ICM temperature and X-ray luminosity increase around the on-going phase, the so-called merger boost, and subsequently decrease at the post-merger phase because of adiabatic expansion. According to Ricker and Sarazin's (2001) simulations, the increment in temperature and the X-ray luminosity could be a factor of about four and 10, respectively, for a head-on equal mass merger, and the time scale over which luminosity and temperature are boosted is of the order of the sound-crossing time. The sub-cluster gradually decelerates before reaching a turn-around distance, and then it starts the second impact. The increase of X-ray luminosity due to the merger boost at the second core passage is much smaller than that at the first one, only 30–70% for a head-on equal mass merger (Ricker & Sarazin 2001). The consecutive time scale of cluster mergers is on the order of a gigayear and is much shorter than the dynamical time. Due to the merger boost effect, a certain probability of finding merging clusters through X-ray observations is biased toward the on-going phase. Therefore, most previous studies focus on on-going mergers, while studies of pre-/post-phase merging clusters are very limited. In order to understand the overall process of cluster mergers, it is vitally important to study cluster mergers at various merger phases using an homogeneous merging cluster sample with a selection function independent of the merger boost of the ICM (Okabe et al. 2019).

The Hyper Suprime-Cam Subaru Strategic Program (HSC-SSP; Aihara et al. 2018a, 2018b; Bosch et al. 2018; Coupon et al. 2018; Furusawa et al. 2018; Huang et al. 2018; Kawanomoto et al. 2018; Komiyama et al. 2018; Miyazaki et al. 2018; Aihara et al. 2019) is an on-going wide-field optical imaging survey composed of three layers of different depths (Wide, Deep, and UltraDeep). The Wide layer is designed to obtain five-band (*grizy*) imaging over 1400 deg^2. The HSC-SSP Survey achieves both excellent imaging quality ($\sim$0.7 arcsec seeing in the *i* band) and deep observations ($r \lesssim 26$ AB mag). Therefore, the HSC-SSP Survey currently has the best performance to search for galaxy clusters and to measure their weak-lensing masses (for review, Pratt et al. 2019). Oguri et al. (2018) constructed a cluster catalogue using the Cluster finding Algorithm based on Multi-band Identification of Red-sequence gAlaxies (CAMIRA; Oguri 2014). The catalogue contains $\sim$1900 clusters at $0.1 < z < 1.1$ with richness larger than $N = 15$ in the $\sim$240 deg^2 HSC-SSP S16A field. Okabe et al. (2019) found $\sim$190 major-merger candidates using a peak-finding method with galaxy maps of the CAMIRA clusters and confirmed that the sub-cluster mass is more than one-tenth of the main cluster mass from the stacked weak-lensing analysis. The galaxy distribution provides us with unique and ideal information to construct a homogeneous sample of major mergers because distributions of long-lifetime galaxy subhalos are similar to those of dark matter subhalos (Okabe & Umetsu 2008; Okabe et al. 2014). The sample can cover from pre- to post-mergers in various dynamical stages. However, it is difficult to distinguish merging phases only from optical data. Therefore,

X-ray follow-up observations of optically selected merging clusters are critical to the identification of cluster merger phases as well as to the study of cluster merger physics, especially at the non-on-going phase.

HSC J085024+001536 is one of the major-merger candidates (Okabe et al. 2019) at (RA, Dec) = $(8^h 50^m 23^s.9, 0°15'36''.4)$ (J2000.0). The richness of cluster members is $N \sim 60$, and its photometric redshift is $z = 0.1966$ (Oguri et al. 2018). The brightest cluster galaxy (BCG) in HSC J085024+001536 corresponds to SDSS J085027.77+001501.5, the redshift of which is $z = 0.19608$ (Driver et al. 2011).

In this paper, we present the analysis results of HSC J085024+001536 as the first object of joint X-ray, optical, and weak-lensing study of optically selected merging clusters from the HSC-SSP Survey. Using optical data, we investigate the galaxy density distribution of HSC J085024+001536 (subsection 2.1), construct a weak-lensing mass map, and measure its weak-lensing mass (subsection 2.2). We then search for any residual structures in X-ray images (subsection 2.5), and any unique temperature structures by X-ray spectral analysis (subsection 2.6). Based on these results, we discuss the spatial distribution of the ICM and the merging history (section 3).

Throughout this paper, we adopt a Hubble constant of $H_0 = 70\,\mathrm{km\,s^{-1}\,Mpc^{-1}}$, and cosmological density parameters of $\Omega_{m,0} = 0.27$ and $\Omega_{\Lambda,0} = 0.73$. In this cosmology, $1'$ corresponds to 196 kpc at the redshift of $z = 0.1966$. All error ranges are 68% confidence intervals unless otherwise stated.

2 Data analysis and results

2.1 Galaxy density distribution

We first generated the galaxy density distribution map using the Subaru HSC-SSP S19A data, i.e., the data obtained until the first semester of 2019 (Aihara et al. 2019) . We selected red-sequence galaxies with z-band magnitudes brighter than 24 ABmag in the color–magnitude plane, following Nishizawa et al. (2018) and Okabe et al. (2019). We adopt the smoothing scale of 200 h_{70}^{-1} kpc. The green contours in figure 1 show the galaxy density distribution overlaid on a Subaru-HSC i-band image. The galaxy density distribution has two peaks, the north-west peak and the south-east peak (hereafter the NW peak and SE peak, respectively). The NW peak corresponds to the galaxy SDSS J085020.60+001733.8. The SE peak is offset to the north-west from the brightest cluster galaxy (BCG; SDSS J085027.77+001501.5) because the BCG is too bright for the Subaru telescope and the BCG and its surrounding galaxies are missed by photometry flags.

Figure 1 also shows the distribution of galaxies that have a spectroscopic redshift of $0.188 < z < 0.201$ in the Galaxy
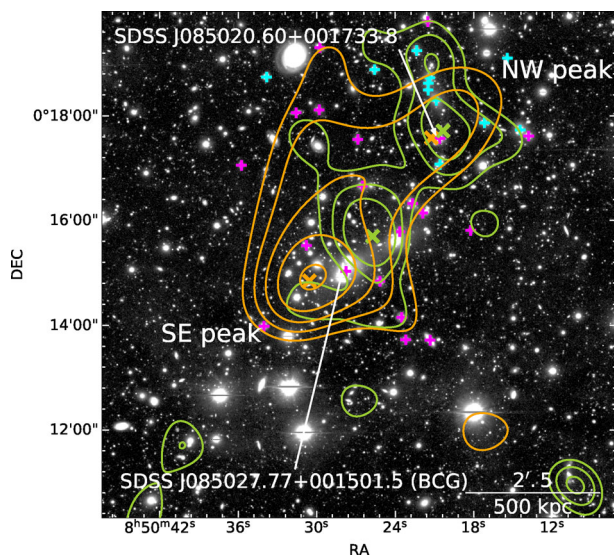

Fig. 1. Contours of the galaxy density distribution (green) and of the weak-lensing mass map (orange), superposed on the optical image observed with Subaru/HSC. The green and orange x-marks show the peaks of the galaxy density and the weak-lensing mass, respectively. Contours of the galaxy density and the weak-lensing mass are smoothed with $\sigma = 200$ and 400 kpc, respectively. The light blue and magenta + signs show the distribution of galaxies which have redshifts of $0.188 < z < 0.193$ and $0.193 < z < 0.201$, respectively, taken from the GAMA DR3 spectroscopic redshift catalogue (Baldry et al. 2018). (Color online)

and Mass Assembly (GAMA) survey Data Release 3 (DR3) catalogue (Baldry et al. 2018). Redshifts of the galaxies around the SE peak and NW peak are $z \sim 0.197$ and $z \sim 0.191$, respectively.

2.2 Weak-lensing analysis

We use the re-Gaussianization method (Hirata & Seljak 2003), which is implemented in the HSC pipeline (see details in Mandelbaum et al. 2018) to measure galaxy shapes. We select only galaxies satisfying the full-color and full-depth criteria from the HSC galaxy catalogue for both our precise shape measurements and photometric redshift estimations.

We compute a weak-lensing (WL) mass reconstruction, a so-called mass map, following Okabe and Umetsu (2008). The mass map does not assume any mass models and thus is complementary to the model fitting. We adopt the full width at half-maximum (FWHM) = 400 h_{70}^{-1} kpc smoothing scale. Figure 1 compares the galaxy density and weak-lensing mass map. The weak-lensing mass map elongates from north-west to south-east. The main, SE peak coincides with the BCG position within the smoothing scale. The NW weak-lensing peak is associated with the NW peak of the galaxy density distribution.

We carry out a Navarro–Frenk–White (NFW) model (Navarro et al. 1996) fitting with a free central position using a two-dimensional shear pattern (Oguri et al.

Table 1. Best-fitting parameters obtained by the two-dimensional weak-lensing analysis.

Parameter	SE peak	NW peak
RA [°]	$132.635^{+0.005}_{-0.013}$	$132.588^{+0.006}_{-0.009}$
Dec [°]	$0.256^{+0.005}_{-0.008}$	$0.292^{+0.012}_{-0.008}$
M_{500} [$10^{14} h_{70}^{-1} M_\odot$]	$1.35^{+0.76}_{-0.62}$	$0.52^{+0.69}_{-0.36}$
c_{500}	$2.56^{+0.17}_{-0.07}$	$2.80^{+0.51}_{-0.19}$
r_{500} [arcmin]/[kpc]	$3.67^{+0.59}_{-0.68}/734^{+118}_{-136}$	$2.66 \pm 0.87/533 \pm 173$
$r_{\rm s}$ [arcmin]/[kpc]	$1.43^{+0.28}_{-0.33}/287^{+56}_{-66}$	$0.95^{+0.40}_{-0.41}/190^{+80}_{-81}$

2010; Okabe et al. 2011) to measure the mass of the main and subhalos. The formulation of weak-lensing mass measurements is described in detail in the Appendix. The three-dimensional mass density profile of the NFW profile (Navarro et al. 1996) is expressed as

$$\rho_{\rm NFW}(r) = \frac{\rho_{\rm s}}{(r/r_{\rm s})(1 + r/r_{\rm s})^2}, \tag{1}$$

where $r_{\rm s}$ is the scale radius, and $\rho_{\rm s}$ is the central density parameter. The NFW model is also specified by the spherical mass, $M_\Delta = 4\pi \Delta \rho_{\rm cr} r_\Delta^3 / 3$, and the halo concentration, $c_\Delta = r_\Delta / r_{\rm s}$. Here, r_Δ is the overdensity radius, and we use $\Delta = 500$. Table 1 shows the best-fitting NFW parameters for the NW and the SE mass structures. The main cluster is associated with the SE peak as shown in the mass map (figure 1). The best-fitting center positions of the SE and NW peaks agree with the BCG and the NW bright galaxy, SDSS J085020.60+001733.8, respectively. The mass ratio of the sub-cluster to the main cluster is $0.32^{+0.75}_{-0.23}$, suggesting that the cluster is a major merger. The NW sub-cluster is offset by ~ 700 kpc from the main cluster center.

2.3 X-ray data reduction

Table 2 shows the information of the XMM-Newton archival data used in this paper. The observation was carried out by the medium filter for MOS (Turner et al. 2001) and the thin filter for pn (Strüder et al. 2001).

We reduced the data using the Science Analysis System (SAS) version 18.0.0, following the SAS threads,[1] and also Miyaoka et al. (2018). We filtered the raw data and extracted the cleaned events by the conditions of FLAG=0 and PATTERN ≤ 12 for MOS, and FLAG=0 and PATTERN ≤ 4 for pn. The net clean exposure times became 50.9, 53.1, and 38.9 ks for the MOS1, MOS2, and pn data, respectively, from the raw exposure time (62.9 ks). Point sources were then removed using the SAS task `cheese`. We also compared X-ray images with an optical image and manually removed the remaining point-like sources.

[1] ⟨https://www.cosmos.esa.int/web/xmm-newton/sas-thread-esasimage⟩.

We used `mos_spectra` and `pn_spectra` to generate spectral files and redistribution matrix files (RMFs). As for the telescope responses, extended auxiliary response files (ARFs) were generated using the `arfgen` command. Among the non-X-ray background (NXB), spectra and images of the quiescent particle background (QPB) were estimated and generated using the `mos_back` and `pn_back` commands. On the other hand, images of the soft proton contamination were generated using the `proton` command with the best-fitting indices and normalizations, determined by spectral fitting using a broken power-law model for this background component.

2.4 X-ray image

The left-hand panel of figure 2 shows an XMM-Newton image in the 0.4–4.0 keV band. Extended X-ray emission is clearly detected from HSC J085024+001536 for the first time. The net counts after subtracting the QPB, in the elliptical region of HSC J085024+001536 defined in the left-hand panel of figure 2, are 5300 in the 0.3–11 keV band for the MOS2, and 12260 in the 0.4–11 keV band for the pn, respectively. Note that three other clusters (HSC J084950+002334, HSC J085106+003140, and GAMA 215032) are also detected in the same field of view. The right-hand panel of figure 2 shows a close-up view of HSC J085024+001536, overlaid with contours of the weak-lensing mass map shown in figure 1. The diffuse X-ray emission concentrates on the main cluster of the SE peak, and it is very faint around the NW peak of the weak-lensing mass map.

2.5 Residual structures in the X-ray image

We fit the X-ray surface brightness image in the 0.4–4.0 keV band to find evidence of a cluster merger. We adopt a multi-component model to describe the complexity of X-ray surface brightness distribution. We consider two components of diffuse emission (hereafter, ICM-West and ICM-East). Each component is described with a two-dimensional elliptical β model for diffuse emission,[2]

$$S_\beta^e(x, y) = S_0 \left[1 + \frac{X(x, y)^2 (1-e)^2 + Y(x, y)^2}{r_{\rm core}^2 (1-e)^2} \right]^{-3\beta + 1/2}, \tag{2}$$

$$X(x, y) = (x - x_{\rm c}) \cos\theta + (y - y_{\rm c}) \sin\theta, \tag{3}$$

[2] We also fitted the image with a single-β model and three-β models (plus point sources and a constant background model as shown in equation (5). In the one-β case, the C-statistic value was 64512 and large residuals remained near the center, compared with 64339 for the two-β case. In the three-β case, the C-statistic value, 64309, was comparable to that for the two-β case, and the global structures were the same. Therefore, the two-β case is valid.

Table 2. XMM-Newton archival data. The flare time is removed from the exposure time.

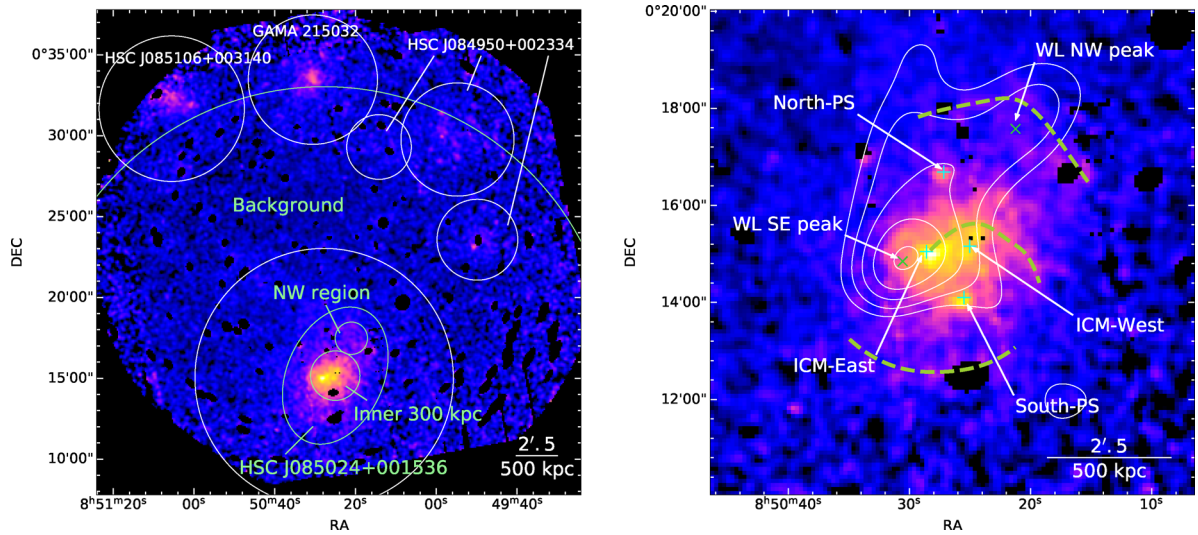| Obs ID	Target name	Start time [UT]	Exposure time (MOS1/MOS2/pn) [ks]	RA	Dec
761730501	J0850+0022	2015-10-18 09:45:40	50.9 / 53.1 / 38.9	$08^h 50^m 27\overset{s}{.}88$	$-00°22'55\overset{''}{.}0$

Fig. 2. (Left) X-ray image in the 0.4–4.0 keV band after subtracting the NXB, correcting exposure-time, and smoothing with $\sigma = 5''$. MOS1, 2, and pn images were merged. The NXB includes QPB and residual soft proton contamination, generated by the SAS tasks `mos_back/pn_back` and `proton`, respectively. HSC J085024+001536 is detected to the south in the field of view (green ellipse). HSC J084950+002334, HSC J085106+003140, and GAMA 215032 are also detected. Since HSC J084950+002334 is a low-redshift (0.17) and low-richness (~15) cluster (Oguri et al. 2018), the member galaxies are widely and shallowly distributed. The three X-ray emissions are associated with the member galaxy distribution or the brightest cluster galaxy. As described in subsection 2.6, a region of sky background is shown by the green arc, excluding the regions shown with white circles. (Right) Close-up view of HSC J085024+001536. The weak-lensing mass contours are also shown with the peak positions as the green x marks (see figure 1 and table 1). Green crosses show the positions of the WL mass map peaks, blue crosses show positions of the X-ray brightness peaks, and green dashed curves indicate the residual arc-like ridges. See subsection 2.5 for details. (Color online)

$$Y(x, y) = (y - y_c) \cos\theta - (x - x_c) \sin\theta \qquad (4)$$

where r_{core} is the core radius, β is the outer slope, e is the ellipticity, θ is the orientation angle and x_c, y_c are the coordinates of the center position. The parameter range for the center position is limited within $50'' \times 50''$ square boxes from the X-ray peaks. Since the outer slope β and the ellipticity e for the ICM-East component cannot be constrained, we fix $\beta = 1$ and $e = 0$, respectively. We additionally introduce delta functions (S_{PS}) to represent two point sources (hereafter, North-PS and South-PS), and a constant (S_b) to represent the sky-background component. The total surface brightness distribution, S_X, is described by

$$S_X = S^e_{\beta, West} + S^e_{\beta, East} + S_{PS, North-PS} + S_{PS, South-PS} + S_b. \qquad (5)$$

We use Sherpa (Freeman et al. 2001) in CIAO version 4.11 (Fruscione et al. 2006) for image fitting. We determine the fitting area as a $12'$ square region centered at the BCG. Source distribution models were convolved with an exposure map, and a telescope's point spread function (PSF) map which was generated at the energy of 2.2 keV and at the BCG position using the `psfgen` tool. The observed images, PSF maps, exposure maps, and NXB images were rebinned so that the pixel size became $5''$. The images of the three detectors were fitted simultaneously using the C-statistic (Cash 1979). The normalization of each component and the constant for the background were linked between MOS1 and MOS2 images because the cluster center is on the dead chip of MOS1.

Table 3 summarizes the best-fitting parameters of the image fitting, and figure 3 shows contours of the best-fitting models overlaid with the X-ray image. The best-fitting positions of ICM-West, ICM-East, North-PS, and South-PS are also shown in figure 3. ICM-East coincides with the BCG position, and ICM-West is the X-ray morphological center. Since instrumental Al Kα and Si Kα lines are predominant in the low surface brightness region, we evaluated the influence of these lines by excluding the 1.3–1.9 keV energy range. As a result, the C-statistic was greatly improved (C-statistic = 64339 → 62146, d.o.f unchanged), but the best-fitting values were unchanged within errors. When we fitted X-ray images after subtracting images of the soft proton contamination generated by the SAS task

Table 3. Best-fitting parameters obtained by fitting the X-ray image.

Parameter	ICM-West	ICM-East	North-PS	South-PS	Background
r_{core} [arcmin]/[kpc]	68^{+10}_{-5} / 223^{+34}_{-15}	43 ± 4 / 140^{+12}_{-13}	-	-	-
β	$0.51^{+0.04}_{-0.02}$	1.00(fix)	-	-	-
e	0.32 ± 0.02	0.00(fix)	-	-	-
θ [rad]	1.16 ± 0.04	0.00(fix)	-	-	-
RA [°]	132.6043 ± 0.0001	132.6191 ± 0.0001	$132.6132^{+0.0011}_{-0.0003}$	$132.6062^{+0.0012}_{-0.0002}$	-
Dec [°]	0.2527 ± 0.0005	0.2507 ± 0.0005	$0.2781^{+0.0002}_{-0.0012}$	$0.2350^{+0.0002}_{-0.0012}$	-
Norm$_{MOS1}$ [c s^{-1} deg^{-2}]	$14.1^{+0.9}_{-1.8}$	$15.8^{+2.3}_{-1.9}$	159^{+43}_{-39}	220^{+56}_{-53}	$0.73^{+0.04}_{-0.05}$
Norm$_{MOS2}$ [c s^{-1} deg^{-2}]*	$13.9^{+0.8}_{-1.6}$				
Norm$_{pn}$ [c s^{-1} deg^{-2}]	$11.8^{+0.6}_{-1.1}$	$11.7^{+1.2}_{-1.0}$	96^{+19}_{-18}	197^{+31}_{-29}	0.83 ± 0.03
C-statistic	64339.3				
d.o.f	41669				
C-statistic/d.o.f	1.544				

*Norm (MOS2, W535-West) × Norm (MOS1, each component)/Norm (MOS1, W535-West).

proton, the parameters of the β models were unchanged within errors because the observational data is not significantly affected by the flare. Note that we confirmed that the position and energy-dependence of the PSF shape has a negligible influence on the fitting results.

The left-hand panel of figure 4 shows the residual image after subtracting the best-fitting model shown in table 3 and in figure 3 from the X-ray image. There are arc-like residual structures in the cluster center, and to the north and to the south of the cluster center.[3] Note that these structures are clearly found in the residual image of each detector. We confirmed that the significance levels of these structures are $\sim 1\sigma$ for the central structure, and ~ 2–3σ for the north and the south structures in the stacked residual image, respectively. Based on the location of the residual arc-like structures, four sectors were defined as shown in the right-hand panel of figure 4: north (25°–110°), east (110°–215°), south (215°–300°), and west (300°–25°).

Figure 5 shows radial profiles of the X-ray surface brightness after subtracting the NXB in the north and the south sectors shown in figure 4. Large excess is shown at the distance of 40–90 kpc and 450–650 kpc in the north sector, and at 450–650 kpc in the south sector. The significance levels of these excesses are 2.5σ, 6.6σ, and 3.6σ, respectively. The excess ridges are located at ~ 80 kpc and ~ 550 kpc from the ICM-West (figure 4). The south and north ridges are tangentially elongated along ~ 400 and ~ 650 kpc length, respectively. Although these excesses can be represented by the cold front density jump model given

[3] To check the robustness of the detected excesses with respect to the underlying model, we tested β of the ICM-East fixed at 0.7, and β free. We also tested that the ellipticity e set free, but e became 0. In all cases, the arc-like structures were unchanged. They were also unchanged in the case of a single-β model and three-β models. In fact, these features are weakly visible in the raw image (see the right-hand panel of figure 2).
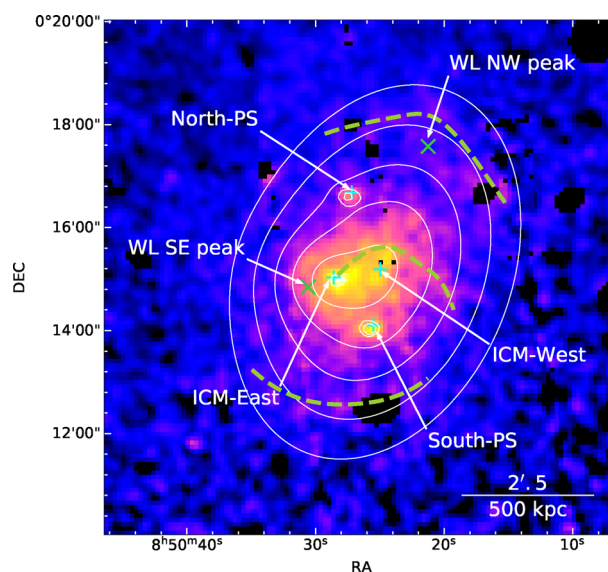

Fig. 3. X-ray image in the 0.4–4.0 keV band, overlaid with contours of the best-fitting models described in table 3, convolved with the telescope PSF, and smoothed with $\sigma = 5''$. The X-ray image is the same as the right-hand panel of figure 2. (Color online)

by equation (A4) of Owers et al. (2009), the parameters were not well-constrained due to limited photon statistics.

2.6 Spectral features of the ICM

To understand the ICM properties, we first fitted the EPIC spectra of the three regions shown in the left-hand panel of figure 2. The first is an ellipsoid region centered at ICM-West, which has a semi-major axis of $4'.4$, a semi-minor axis of $3'$, and is tilted by 1.16 rad (66°) based on the X-ray image fitting result shown in table 3. We refer to it as the entire region of the cluster. The second is a circle of 300 kpc radius centered at the ICM-West center, referred
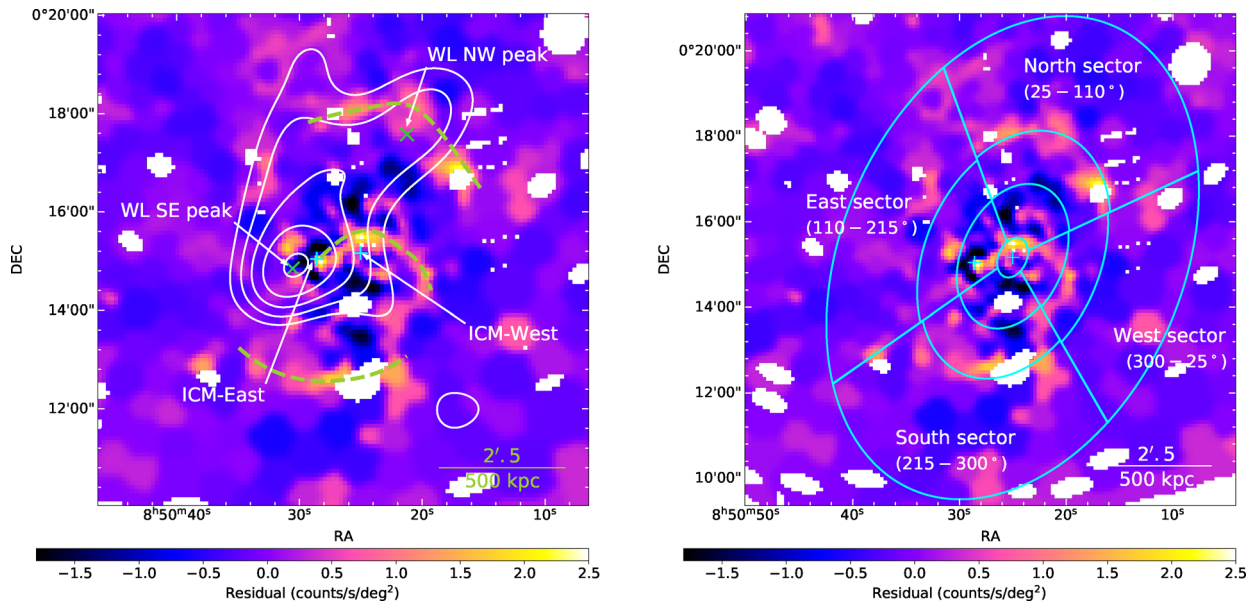
Fig. 4. (Left) Residual map after subtracting the best-fitting models shown in table 3 and figure 3 from the X-ray image. We stacked MOS1, MOS2, and pn residual images. The stacked residual image is binned into a Weighted Voronoi Tesselation (WVT) algorithm (Diehl & Statler 2006), where each region contains at least 40 counts in the original image. The stacked residual image is smoothed with $\sigma = 5''$ for visual purpose. White contours show the weak-lensing mass map, which are the same as those in the right-hand panel of figure 2. Light-blue crosses show the best-fitting positions of ICM-West and ICM-East. Green dashed curves are added to emphasize the residual arc-like ridges. (Right) Definition of regions. Four sectors are defined taking into account locations of the residual arc-like ridges. They are referred to as north (25°–110°), east (110°–215°), south (215°–300°), and west (300°–25°). Each sector is further divided into four annular regions in spectral analysis in subsection 2.7. (Color online)
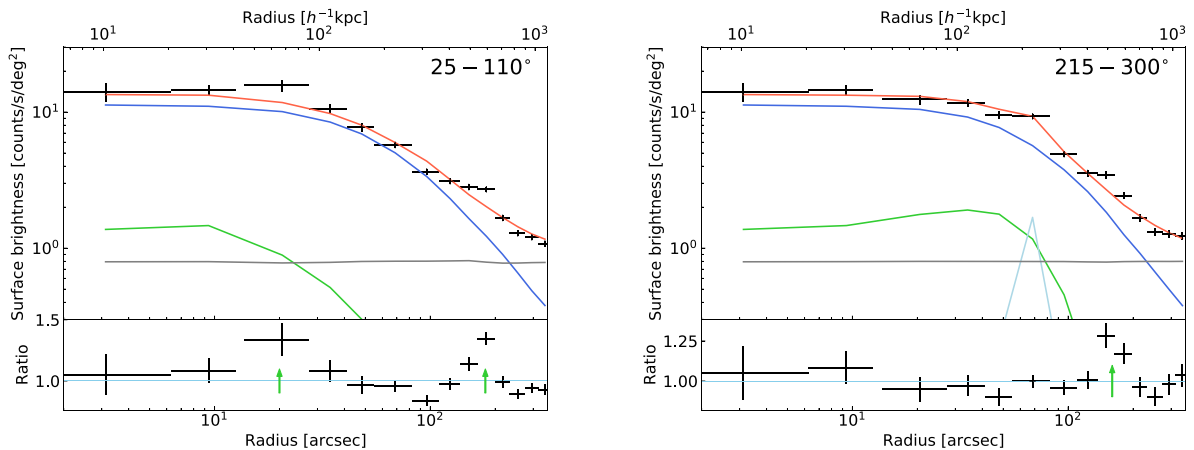
Fig. 5. X-ray surface brightness profiles in the north sector (left) and in the south sector (right) defined in the right-hand panel of figure 4 as a function of projected distance from the ICM-West center. The NXB was subtracted, the exposure time was corrected, and MOS1, 2, and pn data were merged. The dark-blue, green, light-blue, and gray solid curves show the contribution of ICM-West, ICM-East, South-PS, and sky-background components, respectively, which are calculated using the best-fitting models shown in table 3 and figure 3. The red curves are their sum. The lower section of each panel shows the residuals between the data and the red model curve. The green arrows show two excesses in the north sector and one excess in the south sector. (Color online)

to as the inner 300 kpc region. The third region is a circular NW region of 1′ radius from the best-fitting NW mass peak position determined by the weak-lensing analysis, referred to as the NW region. The background region is defined as an annular region with a radius of 8′–18′ from the BCG, but excluding regions containing other objects as shown by white circles in figure 2.

Among the NXB, the QPB spectra were estimated using the SAS tasks `mos_back` and `pn_back`. The energy band is set to be 0.3–11.0 keV and 0.4–11.0 keV for the MOS and pn spectra, respectively. ARFs for extended sources were made, assuming that the surface brightness is constant within each region. Spectral files are rebinned so that each bin contains at least 10 counts for the entire cluster region, one count for
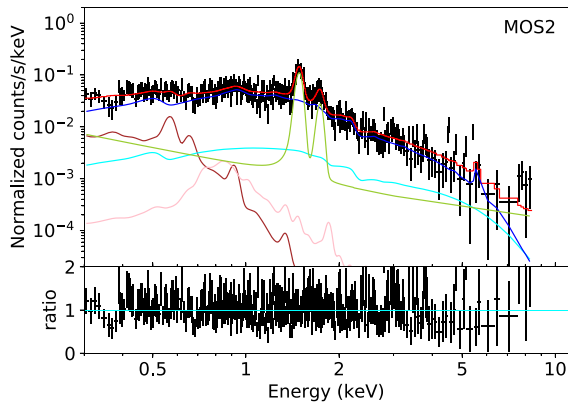
Fig. 6. QPB-subtracted spectra and best-fitting models of the MOS2 from the entire cluster region. The dark-blue, brown, pink, light-blue, and green spectra show the ICM, LHB, MWH, CXB, and unsubtracted NXB (instrumental fluorescent lines and residual soft proton contamination) component, respectively. The red line shows the sum of them. (Color online)

the NW region, and 20 counts for the background region, respectively.

XSPEC version 12.11.0 (Arnaud 1996) was used for spectral fitting, with C-statistic for finding the best-fitting parameters. We adopt the APEC version 3.0.9 (Smith et al. 2001) as a model for emission from the ICM, using the solar abundance table by Lodders and Palme (2009). As a photoelectric absorption model, phabs is utilized with the column density fixed at 3.19×10^{20} cm^{-2} based on the Leiden/Argentine/Bonn (LAB) survey (Kalberla et al. 2005). Following Snowden et al. (2008), background components of the Local Hot Bubble (LHB), the Milky Way Halo (MWH), the Cosmic X-ray Background (CXB), and NXB contribution other than the QPB, i.e., instrumental lines of Al Kα, Si Kα for MOS, and Al Kα, Cu Kα, Kβ, Ni Kα, and Zn Kα for pn, and residual soft proton contamination (De Luca & Molendi 2004; Kuntz & Snowden 2008; Freyberg et al. 2004; Snowden et al. 2004; Carter & Sembay 2008), are represented by models. Spectra of the source regions and the background regions are fitted simultaneously. Parameters among detectors were linked. The redshift was fixed at the cluster photometric redshift $z = 0.1966$ (Oguri et al. 2018).

Figure 6 shows the spectra and the best-fitting models of the entire cluster region, and table 4 summarizes the best-fitting parameters of the ICM component in the entire region, the inner 300 kpc region, and the NW region. The best-fitting temperature of the entire ICM was 3.15 ± 0.14 keV. Note that, when we adopted a two-temperature model, we could not determine the temperature ($kT_1 = 1.70^{+0.37}_{-0.39}$ keV, $kT_2 < 4.27$ keV), and the C-statistic was almost unchanged from the one-temperature model fitting ($1781.45 \rightarrow 1778.52$). The temperature of the NW region is $kT = 2.06^{+0.35}_{-0.26}$ keV, which is lower than that of the entire

Table 4. Best-fitting spectral parameters of the entire region, the inner 300 kpc region, and the NW region.

Parameter	Entire region	Inner 300 kpc region	NW region
kT [keV]	3.15 ± 0.14	$3.42^{+0.25}_{-0.17}$	$2.06^{+0.35}_{-0.26}$
Abundance [$Z_\odot$]	0.32 ± 0.074	$0.36^{+0.10}_{-0.09}$	$0.58^{+0.33}_{-0.23}$
Redshift		0.1966 (fixed)	
Norm (10^{-6})	$8.56^{+0.32}_{-0.31}$	44.8 ± 2.0	$17.0^{+3.0}_{-2.8}$
C-statistic	1781.45	1941.51	1407.56
d.o.f	2046	2334	1593
C-statistic/d.o.f	0.871	0.832	0.884

ICM. Note that this region is also contaminated with a component of the residual arc-like structure described in subsection 2.5, and its contribution cannot be ignored. Thus, we cannot clearly constrain the spectral parameters of the ICM associated with the NW peak.

2.7 Radial profiles of temperature, density, pressure, and entropy

We carry out spectral fitting considering the projection effect, and compute three-dimensional radial profiles of the temperature, the electron density, the gas pressure, and the entropy in the four sectors defined in figure 4. Each sector is divided into four annular regions. We adopt a full ellipse for the innermost region because of the limited number of photons and use a total of 13 regions for spectral fitting. For each projected region, we calculate volumes of the shells in the same line of sight to the region. In deprojection technique, we assume the following geometry; a prolate spheroid aligned with the major and minor axes of the best-fitting ellipse (table 3) on the sky plane and the uniform ICM distribution in each shell of the spheroid. The dead area and the bad pixels of the detectors are properly excluded from the volumes. Weighting factors are calculated by volume ratios, and the 13 spectral files are fitted simultaneously by multiplying the weighting factors. The abundance is linked between all regions.

Figure 7 shows the resulting three-dimensional profiles for gas properties in the four sectors. We compare the temperature profiles in the east sector (top second left-hand panel) and the west sector (top right-hand panel) with the averaged temperature profile of 13 nearby relaxed clusters [Vikhlinin et al. 2005, equation (2)] with $\langle kT \rangle = 3.15$ keV and find an agreement. In contrast, the temperature in the 350–550 kpc region of the north sector ($1.47^{+0.15}_{-0.14}$ keV) is lower than the temperature in the 550–1000 kpc region of the same sector ($2.82^{+0.54}_{-0.37}$ keV), and than the averaged profile for nearby relaxed clusters (Vikhlinin et al. 2005). The low-temperature region corresponds to the region containing the inner half of the arc-like residual structure, i.e.,
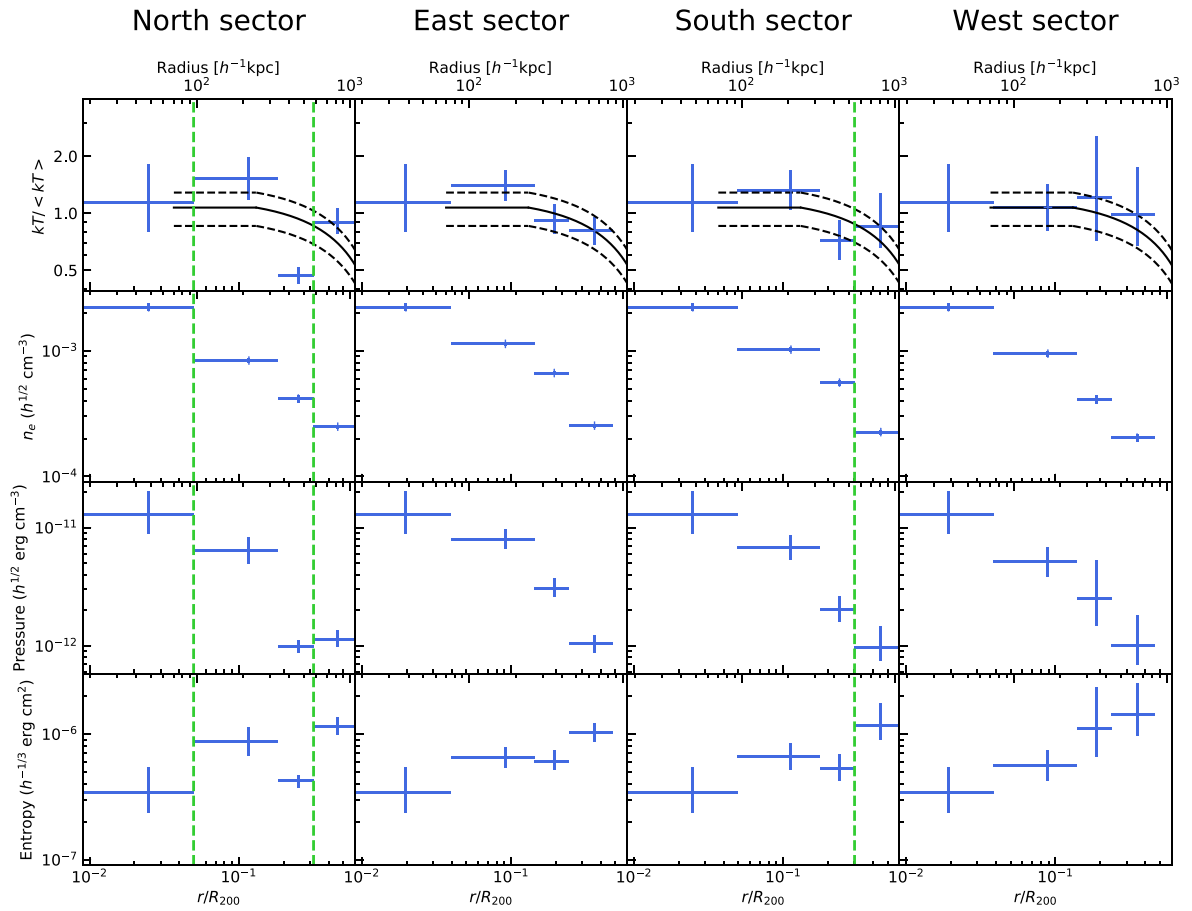
Fig. 7. Three-dimensional radial profiles of the temperature scaled with the average ICM temperature $\langle kT \rangle = 3.15$ keV (first row of panels), electron density (second row), gas pressure (third row), and entropy (fourth row). From left to right, the panels show the north, east, south, and west sectors, respectively. The radii are normalized by the overdensity radius $r_{200} = 1784$ kpc of the main cluster. In the top panels, the black sold curves are the normalized temperature profiles of nearby, relaxed clusters (Vikhlinin et al. 2005) for a reference, and the dashed curves are its 20% scatters. The dashed green lines are the positions of the residual arc-like structure of the surface brightness on the sky. (Color online)

the region inside the candidate front, shown in figures 4 and 5. The gas pressures ($P_{in} = 9.82^{+1.25}_{-1.17} \times 10^{-13}$ erg cm^{-3} and $P_{out} = 1.12^{+0.22}_{-0.15} \times 10^{-12}$ erg cm^{-3}) are nearly constant across the outer residual ridge. On the other hand, the temperatures across the inner residual ridge of the north sector and across the outer residual ridge of the south sector are nearly constant. However, the entropy across all the ridges changes by a factor of 2 (bottom panels).

3 Discussion

The residual map of the X-ray surface brightness (figure 4) and complementary radial profiles (figure 5) show three arc-like excess patterns. The two residual ridges are located at ~550 kpc from the ICM-West center in the north and south regions, and the other ridge is close to the center at ~80 kpc in the north region. The deprojected temperatures across the ridges (figure 7) suggest that the inner temperatures are likely to be somewhat lower than the outer ones. The largest temperature change occurs at the northern

outer ridge, which shows $T_{in}/T_{out} = 0.52^{+0.09}_{-0.11}$. The changes in the other ridges are not significant. Despite the diversity in the temperature properties, the entropy across all ridges changes by more than a factor of 2. This indicates that different originated gases come into contact around the ridges. The entropy profile in the northern direction increases out to ~300 kpc, decreases at ~400 kpc, and increases beyond ~550 kpc. This feature is convectively unstable and thus expected to have a short lifetime. The disturbed gas feature would be dissipated on the order of the sound-crossing time. Given the spatial scale of the entropy pattern, ~550 kpc, and the sound-velocity, $c_s = 616^{+32}_{-30}$ km s^{-1}, its age is expected to be 0.9 ± 0.1 Gyr or greater. A likely perturber inducing the disturbance in the surface brightness is the NW subhalo.

We estimate a gas mass fraction for the NW subhalo within a radius of 1′, which is comparable to r_{2500}, from the NW peak of the weak-lensing mass map. The weak-lensing mass for the NW subhalo is $M_{WL} = 1.7^{+1.4}_{-1.0} \times 10^{13} M_\odot$ from the two-dimensional weak-lensing analysis (subsection 2.2).

The gas density is estimated from the normalization of the APEC model shown in table 4, assuming that it is constant within the same sphere and the filling factor of 1. Then, the gas mass in the sphere is estimated to be $M_{gas} = 6.6^{+0.6}_{-0.5} \times 10^{11} \, M_\odot$. The gas mass fraction in the NW subhalo, $f_{gas} = 4.0^{+2.3}_{-3.3}\%$, is marginally smaller than expected from numerical simulation with active galactic nucleus (AGN) feedback, $f_{gas} = 7.6^{+0.4}_{-0.5}\%$, computed by the weak-lensing mass and the redshift (Planelles et al. 2013). This indicates that a large fraction of the ICM, which had been associated with the NW subhalo, was stripped by the cluster collision. Note that the gas mass fraction obtained here should be regarded as an upper limit, since there are ICM contributions from the main cluster and the north ridge in this region.

The symmetric distribution of the arc-like features around the ICM-West center strongly suggests that these features are due to the sloshing of the central ICM of the main cluster, as suggested by Ascasibar and Markevitch (2006). In this scenario, the NW sub-cluster could play the role of a gas-poor sub-cluster which triggered the disturbance of the gravitational potential including the gas motions.

We estimate a merger time scale from the weak-lensing masses using a simple gravitational interaction (Ricker & Sarazin 2001). We use r_{200} and M_{200} of the SE halo and the NW subhalo in the calculation. We assume a large impact parameter $b = 500 \, \text{kpc}$, since there are features that resemble cold fronts in the simulations with a large impact parameter (e.g., Ricker & Sarazin 2001; Poole et al. 2006). Given these conditions and using equation (31) of Ricker and Sarazin (2001), the relative velocity of the two sub-clusters is $\sim 2000 \, \text{km s}^{-1}$ at the closest impact. Note that the relative line-of-sight velocity of the two sub-clusters determined from the redshift of the member galaxies (subsection 2.1) is $\sim 1300 \, \text{km s}^{-1}$, and there is no major contradiction with our simple estimation. In this case, it takes $\sim 0.12 \, \text{Gyr}$ for the subhalo to reach the current distance ($\sim 700 \, \text{kpc}$) after the closest impact. This estimate is much shorter than the age of the cold front $\gtrsim 0.9 \, \text{Gyr}$ (see the first paragraph in this section). Since the dynamical time from the closest separation to the maximum expansion is $\sim 1.6 \, \text{Gyr}$, which is calculated using equation (31) of Ricker and Sarazin (2001), the total time after the first closest impact is $\gtrsim 3 \text{Gyr}$. Therefore, the cluster is likely to be in the late phase of the cluster merger, at least at the second impact. Again, since the optically-defined merging cluster catalog is unbiased against the cluster merger phase in contrast to X-ray and Sunyaev–Zel'dovich effect observations, X-ray follow-up studies have the advantage to study cluster mergers at various phases.

We also searched for a radio relic or halo using the NRAO VLA Sky Survey data (NVSS; Condon et al. 1998). Although there is radio emission related to the radio galaxy (BCG), we could not find any diffuse radio emission. Since HSC J085024+001536 is a low-mass merger, it would be difficult to detect diffuse radio emissions because of the low energy release (Okabe et al. 2019).

Numerical simulations (Ascasibar & Markevitch 2006) studied the process of the cold front formation. They found that the cold fronts generated by the first core passage can survive and continue to grow by the disturbance of moving subhalos beyond the second core passage. The bottom center panel of figure 3 in Ascasibar and Markevitch (2006) shows multiple spiral structures of the sloshed gas and a cold front, similar to the case of HSC J085024+001536 (figure 4). The simulated image is at 2.8 Gyr after the first core passage, which agrees with our estimation.

Simionescu et al. (2012) found that a large scale cold front exists in the Perseus cluster $\sim 700 \, \text{kpc}$ from the center, and Walker et al. (2018) estimated that its age is $\sim 5 \, \text{Gyr}$. Rossetti et al. (2013) found a cold front at even larger scale (1 Mpc) in A2142. These features are similar to the case of HSC J085024+001536.

4 Summary

We have carried out a joint X-ray, weak-lensing, and optical study of HSC J085024+001536 as a first target of the optically defined merging clusters.

Both the galaxy density and the weak-lensing mass map showed NW and SE peaks. The two-dimensional weak-lensing analysis revealed that the SE component is the main cluster with $M_{500} = 1.35^{+0.76}_{-0.62} \times 10^{14} \, h_{70}^{-1} \, M_\odot$ and the NW component is the sub-cluster with $0.52^{+0.69}_{-0.36} \times 10^{14} \, h_{70}^{-1} \, M_\odot$. The central position of each halo coincides with the brightest galaxy therein. We estimated the gas mass, $6.6^{+0.6}_{-0.5} \times 10^{11} \, M_\odot$, and the weak-lensing mass, $1.7^{+1.4}_{-1.0} \times 10^{13} \, M_\odot$, in a sphere of $1'$ radius from the NW peak. The resulting gas mass fraction, $f_{gas} = 4.0^{+2.3}_{-3.3}\%$, is smaller than predicted by numerical simulation with AGNs (Ascasibar & Markevitch 2006). This is likely because the ICM of the NW peak had been stripped by ram pressure.

The extended X-ray emission around the SE peak has two peaks, the east peak of which coincides with the BCG, and the west peak is the morphological center of the X-ray image. We simultaneously fitted the X-ray image with two-β models and two point-source models and subtracted the best-fitting models from the X-ray image. The residual map clearly showed three arc-like excesses, two of which are located at outer radii. The X-ray spectral analysis, by dividing the cluster region into four sectors, found the

entropy changes across the ridges of the arc-like excesses. In particular, the north large-scale excess represents the temperature change $T_{in}/T_{out} = 0.52^{+0.09}_{-0.11}$, which agrees with the typical feature of cold fronts. Combining with the ram-pressure stripping, the north cold excess is induced by the moving NW subhalo. The south excess is located at the symmetric position of the north excess with respect to the morphological center. The tangentially elongated multiple excesses, their ages, and dynamical time suggests that HSC J085024+001536 is at a late phase merger, at least at the second impact or later, with a non-zero impact parameter.

Appendix. Two-dimensional weak-lensing analysis

We here describe the weak-lensing mass measurement using two-dimensional shear pattern. The dimensional reduced shear $\Delta\Sigma_\alpha$ ($\alpha = 1, 2$) is computed by averaging the measured ellipticity e_α in a kth grid box of $1.'5 \times 1.'5$;

$$\Delta\Sigma_\alpha(\boldsymbol{x}_k) = \frac{\sum_i e_{\alpha,i} w_i \langle \Sigma_{cr}(z_l, z_{s,i})^{-1} \rangle^{-1}}{2\mathcal{R}(\boldsymbol{x}_k)[1 + K(\boldsymbol{x}_k)] \sum_i w_i} \tag{A1}$$

(e.g., Miyaoka et al. 2018; Medezinski et al. 2018a; Okabe et al. 2019, 2021; Miyatake et al. 2019; Murata et al. 2019; Umetsu et al. 2020). The two-dimensional position, $\boldsymbol{x}_k$, is defined by the weighted harmonic mean (Okabe et al. 2016). The inverse of the mean critical surface mass density for the ith galaxy is computed by the probability function $P(z)$ from a machine-learning method (MLZ; Carrasco Kind & Brunner 2014) calibrated with spectroscopic data (Tanaka et al. 2018).

$$\langle \Sigma_{cr}(z_l, z_s)^{-1} \rangle = \frac{\int_{z_l}^\infty \Sigma_{cr}^{-1}(z_l, z_s) P(z_s) dz_s}{\int_0^\infty P(z_s) dz_s}, \tag{A2}$$

where z_l and z_s are the cluster and source redshifts, respectively. The critical surface mass density is $\Sigma_{cr} = c^2 D_s/4\pi G D_l D_{ls}$, where D_l, D_s, and D_{ls} are the angular diameter distances from the observer to the cluster, from the observer to the sources, and from the lens to the sources, respectively. We use background galaxies satisfying $\int_{z_l+0.2} P(z_s) dz_s > 0.98$ (Medezinski et al. 2018b).

The log-likelihood is defined as

$$-2 \ln \mathcal{L}_{WL} = \sum_{\alpha,\beta=1}^2 \sum_{k,m} [\Delta\Sigma_{\alpha,k} - f_{model,\alpha}(\boldsymbol{R}_k)] \boldsymbol{C}^{-1}_{\alpha\beta,km}$$
$$\times [\Delta\Sigma_{\beta,m} - f_{model,\beta}(\boldsymbol{R}_m)] + \ln[\det(C_{\alpha\beta,km})], \tag{A3}$$

where the subscripts α and β denote each shear component. $C_{\alpha\beta}$ denotes the covariance error matrix of shape measurement. The central positions are restricted to full-width boxes $2' \times 2'$ centered on the BCGs. The two-dimensional analysis is good at determining the central positions (Oguri et al. 2010) and measuring masses of multi-components of merging clusters (Okabe et al. 2011, 2015; Medezinski et al. 2016; Okabe et al. 2021). Since the concentration parameter cannot be constrained well, we assume the mass–concentration relation (Diemer & Kravtsov 2015).

References

Aihara, H., et al. 2018a, PASJ, 70, S4
Aihara, H., et al. 2018b, PASJ, 70, S8
Aihara, H., et al. 2019, PASJ, 71, 114

Arnaud, K. A. 1996, in ASP Conf. Ser., 101, Astronomical Data Analysis Software and Systems V, ed. G. H. Jacoby & J. Barnes (San Francisco: ASP), 17

Ascasibar, Y., & Markevitch, M. 2006, ApJ, 650, 102

Baldry, I. K., et al. 2018, MNRAS, 474, 3875

Bosch, J., et al. 2018, PASJ, 70, S5

Carrasco Kind, M., & Brunner, R. J. 2014, MNRAS, 438, 3409

Carter, J. A., & Sembay, S. 2008, A&A, 489, 837

Cash, W. 1979, ApJ, 228, 939

Condon, J. J., Cotton, W. D., Greisen, E. W., Yin, Q. F., Perley, R. A., Taylor, G. B., & Broderick, J. J. 1998, AJ, 115, 1693

Coupon, J., Czakon, N., Bosch, J., Komiyama, Y., Medezinski, E., Miyazaki, S., & Oguri, M. 2018, PASJ, 70, S7

De Luca, A., & Molendi, S. 2004, A&A, 419, 837

Diehl, S., & Statler, T. S. 2006, MNRAS, 368, 497

Diemer, B., & Kravtsov, A. V. 2015, ApJ, 799, 108

Driver, S. P., et al. 2011, MNRAS, 413, 971

Freeman, P., Doe, S., & Siemiginowska, A. 2001, in Proc. SPIE, 4477, Astronomical Data Analysis, ed. J.-L. Starck & F. D. Murtagh (Bellingham, WA: SPIE), 76

Freyberg, M. J., et al. 2004, in Proc. SPIE, 5165, X-Ray and Gamma-Ray Instrumentation for Astronomy XIII, ed. K. A. Flanagan & O. H. W. Siegmund (Bellingham, WA: SPIE), 112

Fruscione, A., et al. 2006, in Proc. SPIE, 6270, Observatory Operations: Strategies, Processes, and Systems, ed. D. R. Silva & E. Rodger (Bellingham, WA: SPIE), 62701V

Furusawa, H., et al. 2018, PASJ, 70, S3

Hirata, C., & Seljak, U. 2003, MNRAS, 343, 459

Huang, S., et al. 2018, PASJ, 70, S6

Kalberla, P. M. W., Burton, W. B., Hartmann, D., Arnal, E. M., Bajaja, E., Morras, R., & Pöppel, W. G. L. 2005, A&A, 440, 775

Kawanomoto, S., et al. 2018, PASJ, 70, 66

Komiyama, Y., et al. 2018, PASJ, 70, S2

Kuntz, K. D., & Snowden, S. L. 2008, A&A, 478, 575

Lodders, K., & Palme, H. 2009, Meteorit. Planet. Sci. Supp., 72, 5154

Mandelbaum, R., et al. 2018, PASJ, 70, S25

Markevitch, M., & Vikhlinin, A. 2007, Phys. Rep., 443, 1

Medezinski, E., Umetsu, K., Okabe, N., Nonino, M., Molnar, S., Massey, R., Dupke, R., & Merten, J. 2016, ApJ, 817, 24

Medezinski, E., et al. 2018a, PASJ, 70, S28

Medezinski, E., et al. 2018b, PASJ, 70, 30

Miyaoka, K., et al. 2018, PASJ, 70, S22

Miyatake, H., et al. 2019, ApJ, 875, 63

Miyazaki, S., et al. 2018, PASJ, 70, S1

Murata, R., et al. 2019, PASJ, 71, 107

Navarro, J. F., Frenk, C. S., & White, S. D. M. 1996, ApJ, 462, 563

Nishizawa, A. J., et al. 2018, PASJ, 70, S24

Oguri, M. 2014, MNRAS, 444, 147

Oguri, M., Takada, M., Okabe, N., & Smith, G. P. 2010, MNRAS, 405, 2215

Oguri, M., et al. 2018, PASJ, 70, S20

Okabe, N., et al. 2016, MNRAS, 456, 4475

Okabe, N., et al. 2019, PASJ, 71, 79

Okabe, N., et al. 2021, MNRAS, 501, 1701

Okabe, N., Akamatsu, H., Kakuwa, J., Fujita, Y., Zhang, Y., Tanaka, M., & Umetsu, K. 2015, PASJ, 67, 114

Okabe, N., Bourdin, H., Mazzotta, P., & Maurogordato, S. 2011, ApJ, 741, 116

Okabe, N., Futamase, T., Kajisawa, M., & Kuroshima, R. 2014, ApJ, 784, 90

Okabe, N., & Umetsu, K. 2008, PASJ, 60, 345

Owers, M. S., Nulsen, P. E. J., Couch, W. J., & Markevitch, M. 2009, ApJ, 704, 1349

Planelles, S., Borgani, S., Dolag, K., Ettori, S., Fabjan, D., Murante, G., & Tornatore, L. 2013, MNRAS, 431, 1487

Poole, G. B., Fardal, M. A., Babul, A., McCarthy, I. G., Quinn, T., & Wadsley, J. 2006, MNRAS, 373, 881

Pratt, G. W., Arnaud, M., Biviano, A., Eckert, D., Ettori, S., Nagai, D., Okabe, N., & Reiprich, T. H. 2019, Space Sci. Rev., 215, 25

Ricker, P. M., & Sarazin, C. L. 2001, ApJ, 561, 621

Rossetti, M., Eckert, D., De Grandi, S., Gastaldello, F., Ghizzardi, S., Roediger, E., & Molendi, S. 2013, A&A, 556, A44

Simionescu, A., et al. 2012, ApJ, 757, 182

Smith, R. K., Brickhouse, N. S., Liedahl, D. A., & Raymond, J. C. 2001, ApJ, 556, L91

Snowden, S. L., Collier, M. R., & Kuntz, K. D. 2004, ApJ, 610, 1182

Snowden, S. L., Mushotzky, R. F., Kuntz, K. D., & Davis, D. S. 2008, A&A, 478, 615

Strüder, L., et al. 2001, A&A, 365, L18

Tanaka, M., et al. 2018, PASJ, 70, S9

Turner, M. J. L., et al. 2001, A&A, 365, L27

Umetsu, K., et al. 2020, ApJ, 890, 148

Vikhlinin, A., Markevitch, M., Murray, S. S., Jones, C., Forman, W., & Van Speybroeck, L. 2005, ApJ, 628, 655

Walker, S. A., ZuHone, J., Fabian, A., & Sanders, J. 2018, Nature Astron., 2, 292

ZuHone, J. A. 2011, ApJ, 728, 54

ZuHone, J. A., Markevitch, M., & Johnson, R. E. 2010, ApJ, 717, 908

Zuhone, J. A., & Roediger, E. 2016, J. Plasma Phys., 82, 535820301